A modified viscous flow law for natural glacier ice: Scaling from laboratories to ice sheets

PNAS RESEARCH ARTICLE | EARTH, ATMOSPHERIC, AND PLANETARY SCIENCES

A modified viscous flow law for natural glacier ice: Scaling from laboratories to ice sheets

Meghana Ranganathan[a,b,1] and Brent Minchew[a]

Edited by David Kohlstedt, University of Minnesota, Minneapolis, MN; received June 21, 2023; accepted April 9, 2024

Glacier flow modulates sea level and is governed largely by the viscous deformation of ice. Multiple molecular-scale mechanisms facilitate viscous deformation, but it remains unclear how each contributes to glacier-scale deformation. Here, we present a model of ice deformation that bridges laboratory and glacier scales, unifies existing estimates of the viscous parameters, and provides a framework for estimating the parameters from observations and incorporating flow laws derived from laboratory observations into glacier-flow models. Our results yield a map of the dominant deformation mechanisms in the Antarctic Ice Sheet, showing that, contrary to long-standing assumptions, dislocation creep, characterized by a value of the stress exponent $n = 4$, likely dominates in all fast-flowing areas. This increase from the canonical value of $n = 3$ dramatically alters the climate conditions under which marine ice sheets may become unstable and drive rapid rates of sea-level rise.

glacier flow | Antarctica | rheology | glaciology

Significance

The rate of ice flow is a primary control on the rate of mass loss from ice sheets and glaciers. Therefore, the model representation for ice flow is critical to projections of future ice sheet and sea-level change. However, the viscous flow law used in ice sheet models does not fully capture the physical mechanisms and the spatial and temporal variations in ice deformation. We present a framework for calculating the ice-viscosity parameters from ice flow conditions, such as stress, ice temperature, and ice crystal size. This framework allows for modeling variations in ice flow in space and time and can be readily incorporated into ice sheet models to improve representation of ice flow and estimates of future sea-level rise.

Changes in mass loss rates from ice sheets [the Antarctic Ice Sheet (AIS) and the Greenland Ice Sheet (GrIS)] are the largest sources of uncertainty in projections of sea-level rise (1). Most of this mass loss from the AIS and half of the mass loss from the GrIS occurs through fast-flowing glaciers and ice streams (2–5), which transport ice from the grounded ice sheet to the ocean. Ice deformation rates help govern the flow of ice and thus changes in mass loss rates (6). Understanding and modeling the mechanisms that govern ice deformation—among the oldest, most enduring, and most foundational questions in glaciology—are necessary for understanding the evolution of ice sheets and other glaciated areas, reliably projecting sea-level rise, and quantifying the associated uncertainties.

Multiple mechanisms allow ice to deform as a viscous fluid (e.g., refs. 7–13). The combined effect of these mechanisms can be modeled by a composite viscous flow law (or viscous constitutive relation) wherein the total (bulk) deformation rate $\dot{\epsilon}$ is the sum of deformation rates from all deformation mechanisms. Laboratory studies provide evidence for four primary deformation mechanisms in glacier ice (14–16): diffusion creep (denoted in this paper by subscript diff), which arises from the diffusion of vacancies in the crystalline lattice or along grain boundaries; grain-boundary sliding (denoted in this paper by subscript gbs), which involves the relative movement of adjacent grains in which the movement occurs in the grain boundary; dislocation creep (denoted in this paper by subscript dis), which entails the motion of defects known as dislocations in the crystalline lattice; and basal slip (denoted in this paper by subscript basal), which encompasses slip along the basal planes of crystals to accommodate grain-boundary sliding. Most of these mechanisms act in parallel, but grain-boundary sliding and basal slip act in series, with the slower of the two limiting the creep rate. Thus, the total rate of deformation, as proposed by Goldsby and Kohlstedt (15), is

$$\dot{\epsilon} = \dot{\epsilon}_{\text{diff}} + \left[\frac{1}{\dot{\epsilon}_{\text{basal}}} + \frac{1}{\dot{\epsilon}_{\text{gbs}}}\right]^{-1} + \dot{\epsilon}_{\text{dis}}. \quad [1]$$

Each term on the right-hand side can be modeled with a power-law relation of the form $\dot{\epsilon}_i = \tilde{A}_i \tau^{\tilde{n}_i}$, where the flow-rate parameters $\tilde{A}_i(T, d)$ are functions of absolute ice temperature T and mean grain size d, and are defined for each of the creep mechanisms listed above such that $i = \text{diff, basal, gbs, dis}$. We refer to the values $\tilde{n}_i$ as stress exponents. Each deformation mechanism has a different value of $\tilde{n}_i$. The effective strain rate $\dot{\epsilon}$ and effective stress τ are the square roots of the second invariants of the respective tensors (*i.e.*, $\tau = \sqrt{\tau_{ij}\tau_{ij}/2}$, where τ_{ij} is the deviatoric stress tensor, $\dot{\epsilon} = \sqrt{\dot{\epsilon}_{ij}\dot{\epsilon}_{ij}/2}$ where $\dot{\epsilon}_{ij}$ is the deformation or strain rate tensor, and summation is implied for repeated indices). Diffusion creep, grain boundary sliding, and basal slip depend on the mean

Author affiliations: [a]Department of Earth, Atmospheric and Planetary Sciences, Massachusetts Institute of Technology, Cambridge 02139, MA; and [b]School of Earth and Atmospheric Sciences, Georgia Institute of Technology, Atlanta 30332, GA

Author contributions: M.R. and B.M. designed research; M.R. performed research; M.R. and B.M. analyzed data; M.R. and B.M. revised the paper; and M.R. wrote the paper.

The authors declare no competing interest.

This article is a PNAS Direct Submission.

[1]To whom correspondence may be addressed. Email: miranganathan@uchicago.edu.

This article contains supporting information online at https://www.pnas.org/lookup/suppl/doi:10.1073/pnas.2309788121/-/DCSupplemental.

Published May 30, 2024.

grain size d^{-m_i}, where $-m_i \leq 0$ varies for each deformation mechanism, indicating that the different mechanisms have different dependencies on grain size. The negative sign of the exponent $-m_i$ indicates that, all else being equal, deformation rates for the respective deformation mechanism decrease with increasing grain size. Dislocation creep does not depend on grain size, and so we set $m_{\text{dis}} = 0$.

Ice-flow models rarely incorporate Eq. **1**. Instead, they use Glen's flow law, a simpler, bulk viscous flow-law defined by a single power-law relation. This flow law defines a relationship between the effective strain rate $\dot{\epsilon}$ and effective deviatoric stress τ such that (17)

$$\dot{\epsilon} = A\tau^n \qquad [2]$$

without elucidating the individual contributions of the different creep mechanisms. Eq. **2** is related to general constitutive relation for viscous fluids $2\eta\dot{\epsilon}_{ij} = \tau_{ij}$ with $\eta = \tau^{1-n}/(2A)$ being (dynamic) viscosity. While the simplicity of Glen's law is attractive for modeling, uncertainties in the values of A and n arise from the complex rheology of ice (illustrated in Eq. **1**) and the challenges in calibrating these parameters at scale in glaciers and ice sheets. In particular, lacking a formal parameterization that captures deformation processes and their effects on A and n, ice sheet models use an assumed value of n and values of A calibrated or inferred from observations for the assumed n (18–23). The most common assumption is $n = 3$ for all ice flow conditions and all model timesteps. While the value of $n = 3$ agrees well with some studies (e.g., refs. 19, 24, and 25), several other studies have inferred values of n between 1 and 5 based on laboratory experiments (9, 15, 17, 26), in situ measurements (19, 27), observational studies using remote-sensing data of the ice sheet surface (28–30), computational inverse methods (31), and models (32). Thus, understanding the relative contributions of different deformation mechanisms, and by extension, reasonable values of A and n, remains an open problem that we seek to address in this work.

The assumed values of n and A in ice-flow models have substantial yet largely unexplored implications for ice sheet and sea-level rise projections. The implications of n for ice sheet dynamics arise from the fact that n is the exponent that governs the sensitivity of viscosity to stress, and viscosity is of paramount importance to ice flow (33). In particular, values of the A and n parameters have profound effects on our conceptualization of the stability of marine ice sheets like the West AIS, a significant contributor to uncertainties in projections of sea-level rise (1) (Fig. 1). Marine ice sheets have beds that are well below sea level and are thought to be unstable when the bed deepens inland (a retrograde bed slope) because ice floats, allowing for a buoyancy-driven feedback, known as the marine ice sheet instability (MISI), that can cause the rapid retreat of the ice sheet (34–37).

MISI can be triggered in idealized models when the combination of ice rheology and climate allows for an unstable steady state when the grounding line (the boundary between grounded and floating ice) is on a retrograde bed slope (Fig. 1*B*, orange dashed curve) (34). To demonstrate the potential effect of n, A values on ice sheet stability, we apply a simple, steady-state model (35) to a commonly used idealized marine ice sheet geometry (Fig. 1). Our results for $n = 2$ to 4, with corresponding values of A taken from the model we describe herein (Fig. 1*B*), show that varying the viscous parameters within the range of known uncertainties changes the relationship between ice mass flux from land to the ocean (a.k.a., the grounding line flux) and the grounding line position enough to introduce or eliminate the potential for MISI under given climate scenarios. For the chosen climate scenario, the model shows an unstable grounding line position on the retrograde bed when $n = 3$, but for $n = 2$ and 4, the grounding line positions are unconditionally stable (Fig. 1*B*, colored curves). There are no climate scenarios under which a marine ice sheet has an unstable grounding line position for all possible A, n pairs. This simple analysis shows that estimates of marine ice sheet stability and, therefore, sea-level rise projections, are highly sensitive to the values of n and A. This creates an urgent need for more accurate and physically justified estimates of A and n in natural glacier

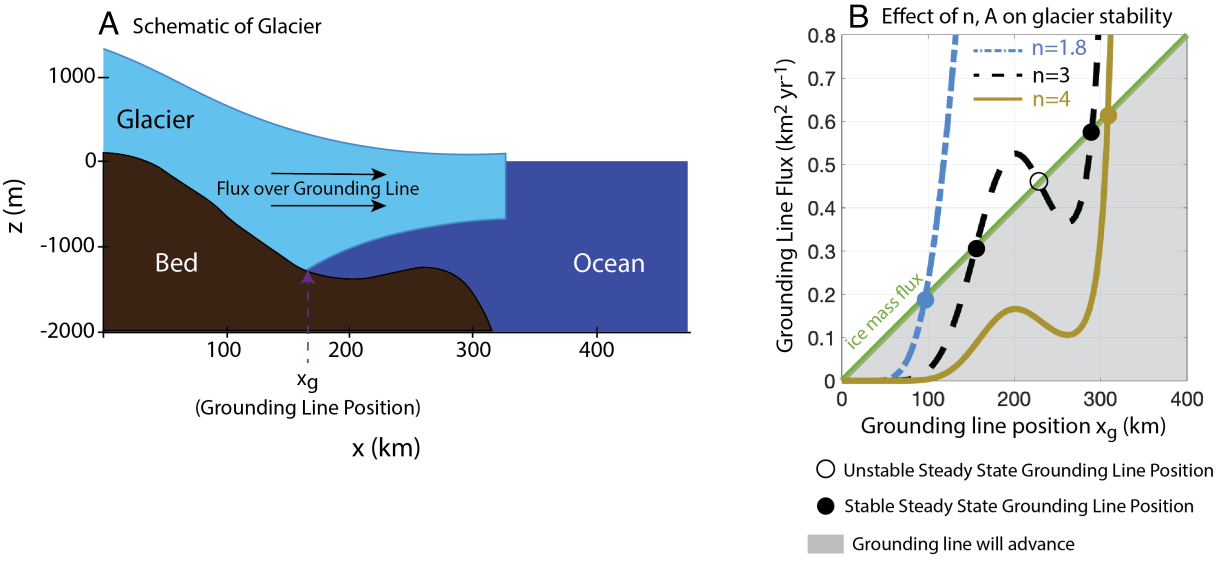

Fig. 1. Effect of n and A on grounding line flux: (*A*) Schematic of a marine ice sheet, denoting the grounding line position and the flux of ice over the grounding line and into the ocean, a value that affects the mass loss from grounded portions of the ice sheet. The bed geometry is defined in ref. 34. (*B*) Estimates of the modeled (35) grounding line position (x-axis) and grounding line flux for $n = 2$ to 4. Intersections of the green, diagonal line (showing mass flux from surface accumulation integrated over the upstream catchment) with the flux curves are the steady-state grounding line positions, with solid and open circles indicating stable and unstable configurations, respectively. Gray background denotes where the grounding line will advance, and white background denotes where the grounding line will retreat.

ice and motivates this study, wherein we present a model for ice deformation that represents the salient known mechanisms of ice deformation (Eq. **1**) and the couplings between ice rheology, temperature, stress, and grain size.

1. A Model for *n* and *A* in Glen's Flow Law

Here, we present a physically derived model for the parameters n and A in Glen's flow law. Our model builds on a series of laboratory experiments (14, 15, 38) that support a composite flow law of the form given in Eq. **1** and provide some estimates of the relevant parameters. While the interpretation and details of these studies are still debated in the literature (12, 39, 40), the framework for and broad takeaways from our model should be valid as they depend on long-standing principles in the rheology of polycrystalline materials and empirical evidence (41–43). We further discuss assumptions made in employing this composite flow law in *Discussion* of this paper. A similar method of estimating n from a composite flow law, derived from Eq. **1**, was presented by Behn et al. (32), in which they applied a different form of a grain size model to investigate depth-varying n in idealized experiments and from ice core data, to establish a physical explanation for the canonical $n = 3$ estimate. Here, we build on this work to explore estimates of n for varying stresses and temperatures using an idealized framework, and across the AIS using satellite observations.

Results from the laboratory studies show that the typical stresses and temperature conditions in ice sheets reduce Eq. **1** to the sum of two mechanisms, dislocation creep and grain boundary sliding. This is because diffusion creep and basal slip-accommodating grain-boundary sliding are most relevant at lower stresses than are typically found in fast-flowing regions (surface velocity $\geq 30\ \mathrm{m\,a^{-1}}$) of ice sheets (14, 15, 38). Therefore, the composite flow law (Eq. **1**) for fast-flowing regions of ice sheets simplifies to

$$\begin{aligned}\dot{\epsilon} &= \dot{\epsilon}_{\mathrm{dis}} + \dot{\epsilon}_{\mathrm{gbs}} \\ &= \tilde{A}_{\mathrm{dis}}(T)\tau^{\tilde{n}_{\mathrm{dis}}} + \tilde{A}_{\mathrm{gbs}}(T)d^{-m_{gbs}}\tau^{\tilde{n}_{\mathrm{gbs}}} \\ &= \tilde{A}_{\mathrm{dis}_0}e^{\frac{-\tilde{Q}_{\mathrm{dis}}}{RT}}\tau^{\tilde{n}_{\mathrm{dis}}} + \tilde{A}_{\mathrm{gbs}_0}d^{-m_{\mathrm{gbs}}}e^{\frac{-\tilde{Q}_{\mathrm{gbs}}}{RT}}\tau^{\tilde{n}_{\mathrm{gbs}}},\end{aligned} \quad [3]$$

where $\tilde{Q}_i$ is the activation energy for mechanism i, $\tilde{A}_{i_0}$ is the prefactor for mechanism i, R is the ideal gas constant, $m_{\mathrm{gbs}} = 1.4$ is the grain size exponent (15), and, as previously discussed, dislocation creep has no dependence on grain size. These relationships between stress and strain rate have been shown to vary with temperature such that there is a sudden increase in deformation rate for both grain-boundary sliding and dislocation creep at a critical transition temperature T^*. This transition is hypothesized to be a result of the onset of premelting (9, 11, 44, 45). This behavior is presently parameterized by a step-change in activation energy and prefactor for each deformation mechanism at a transition temperature, such that for each deformation mechanism, there are two values of activation energy and two values of the prefactor: one for high-temperature creep and one for low-temperature creep. We denote values applicable to low-temperature creep with a superscript$^-$ and values applicable to high-temperature creep with a superscript$^+$. Based on the laboratory experiments by Goldsby and Kohlstedt (15), the transition temperatures are $T^* = 255$ K for grain-boundary sliding and $T^* = 258$ K for dislocation creep. In applying this model, we use values of activation energies and prefactors from ref. 15 (Table 1).

Table 1. Rheological parameters for dislocation creep and grain-boundary sliding

Parameter	Laboratory value	Units
$\tilde{A}^+_{0_{\mathrm{dis}}}$	6×10^{28}	$\mathrm{MPa^{-4}\ s^{-1}}$
$\tilde{A}^-_{0_{\mathrm{dis}}}$	4×10^{5}	$\mathrm{MPa^{-4}\ s^{-1}}$
$\tilde{Q}^+_{\mathrm{dis}}$	181×10^{3}	$\mathrm{J\ mol^{-1}}$
$\tilde{Q}^-_{\mathrm{dis}}$	60×10^{3}	$\mathrm{J\ mol^{-1}}$
$\tilde{A}^+_{0_{\mathrm{gbs}}}$	3×10^{26}	$\mathrm{MPa^{-1.8}\ m^{1.4}\ s^{-1}}$
$\tilde{A}^-_{0_{\mathrm{gbs}}}$	3.9×10^{-3}	$\mathrm{MPa^{-1.8}\ m^{1.4}\ s^{-1}}$
$\tilde{Q}^+_{\mathrm{gbs}}$	192×10^{3}	$\mathrm{J\ mol^{-1}}$
$\tilde{Q}^-_{\mathrm{gbs}}$	49×10^{3}	$\mathrm{J\ mol^{-1}}$

Laboratory values are from ref. 15. Values appropriate for warm ice are labeled with superscript$^+$, while values for cold ice are labeled with superscript$^-$. The transition temperature between warm and cold ice is 255 K for grain-boundary sliding and 258 K for dislocation creep.

We apply this composite flow law to illuminate the spatial variability in Glen's flow law parameters (n and A; Eq. **2**). In practice, this approach may be preferable to incorporating composite flow laws directly into ice-flow models since many of these models incorporate Glen's flow law as presented in Eq. **2**. Using instead the sum of power laws (Eq. **3**) can complicate the internal workings of ice sheet models, not least by requiring ice flow models to become more complex by incorporating grain size models to calculate d. Importantly, the method presented here obviates the need for ice-flow modelers to explicitly solve for grain size, since the grain size model is embedded here within the model results for n, A.

While all deformation mechanisms are active at any given time in deforming ice, the relative contributions of each mechanism set the value of the stress exponent in Glen's flow law n (15, 38). Therefore, the regions where a single mechanism is the dominant contributor to ice deformation can be represented with the respective value of the stress exponent n: Where dislocation creep dominates, $n \to \tilde{n}_{\mathrm{dis}} = 4$, and where grain-boundary sliding dominates, $n \to \tilde{n}_{\mathrm{gbs}} = 1.8$. Where neither mechanism is the dominant contributor, we expect n to take on an intermediate value of $1.8 < n < 4$. The value of the Glen flow-rate parameter A would vary according to the value of n and according to ice temperature and grain size (22).

To compute values of n, we assume that the balance of flow mechanisms (and thus the value of n) vary smoothly in stress-temperature space. This is a generally reasonable assumption given that the value of n is unlikely to change rapidly with strain rate. Using the scalar form of Glen's flow law (Eq. **2**), we calculate n as the slope

$$n = \frac{\log \dot{\epsilon}_{\mathrm{min}} - \log \dot{\epsilon}_{\mathrm{max}}}{\log \tau_{\mathrm{min}} - \log \tau_{\mathrm{max}}}, \quad [4]$$

where $\dot{\epsilon}_{\mathrm{min}} = \dot{\epsilon} - \Delta\dot{\epsilon}$ and $\dot{\epsilon}_{\mathrm{max}} = \dot{\epsilon} + \Delta\dot{\epsilon}$. We compute τ_{min} and τ_{max} from Eq. **3**. Here, we use $\Delta\dot{\epsilon} = 10^{-3}\dot{\epsilon}$ to be the range of effective strain rate for which the flow mechanism may remain approximately constant. The choice of $\Delta\dot{\epsilon}$ does not significantly affect the results for all values $\Delta\dot{\epsilon} \leq 0.1\dot{\epsilon}$ (*SI Appendix*, Fig. S4).

In this model of n, the estimated value of n can change spatially and temporally based on three state variables: the strain rate, ice temperature, and grain size. To calculate n going forward, we employ a combination of observations and physical models to find these state variables. Effective strain rates $\dot{\epsilon}$ are observable from the gradient of surface velocity fields, which are routinely measured from remote sensing observations. To represent the

dependence of deformation rate on ice temperature and grain size, two variables that affect the relative contributions of the deformation mechanisms, we couple Eq. **1** to a steady-state thermomechanical model (46) and a steady-state grain size model (47).

The thermomechanical model represents the vertical advection and diffusion of heat and the dissipation of energy through heat due to viscous deformation. Previous work using this model has shown that regions of rapid deformation (lateral margins of ice streams, basal layers of slower-flowing ice) may contain very warm ice due to the rate of shear heating (46). The steady-state grain size model represents grain size changes due to recrystallization, mechanisms that alter the size, shape, and orientation of ice crystals. This model calculates grain size as the balance between grain growth due to normal grain growth and migration recrystallization and grain reduction due to rotation recrystallization. In regions of rapid deformation and warm ice (such as lateral margins of ice streams and basal layers of slower-flowing ice), migration recrystallization typically dominates, resulting in coarse-grains (47–49). The temperature dependence of this process is parameterized in a way similar to creep, where the rate of migration recrystallization increases significantly above a critical temperature (45, 50). The physical explanation for this critical temperature is the onset of premelt enabling rapid grain boundary migration, which is the same physical process likely responsible for the shift in creep rate at high temperatures. We take the critical temperature in the grain-size model to be $T^* = 255$ K, the same critical temperature found for grain-boundary sliding in ref. 15. This is because both processes are related to grain boundary behavior and, thus, are likely to respond to temperature in a similar way. Further details of these models are discussed in *Materials and Methods* and can be found in the respective publications.

The models of ice temperature and grain size make some critical assumptions, explored in detail in the respective publications and summarized here. First, these models assume that temperature and grain size are in steady state. Therefore, the results shown here can be interpreted as constraining the mechanisms by which ice flows under a steady or slowly varying forcing. For grain size, this is a good assumption (47), but we incur small errors in the temperature field due to the long thermal diffusion time of ice (46). We expect the latter errors to be small relative to other assumptions and model simplifications. Second, they assume that ice advection is vertical, and therefore horizontal (both lateral and along-flow) advection is negligible. We apply this assumption to simplify the advective component of the model. Previous work suggests that our results should be reasonably accurate in Antarctica despite this simplifying assumption (46). We leave adding horizontal advective components into this model framework to future work but note that the deformation maps (Fig. 2) are valid regardless of our assumptions about advection. Only the results we show for some grounded regions of Antarctica can be influenced by our decision to neglect horizontal advection, the implications of which have been discussed in detail in previous publications (46, 51, 52). Finally, the ice temperature and grain size models assume that strain rate is constant with depth, approximating a situation in which the glacier is slipping over soft sediment or the bed is well lubricated with liquid water. This assumption limits our results in Antarctica to fast-flowing glaciers (51, 53–55), though the broader conclusions for the dependence of n and A on stress and temperature should be valid for areas where much of the surface velocity is attributable to deformation within the ice column (i.e., vertical shearing). As far as deformation mechanisms are concerned, we can reasonably assume that vertical shearing is the same as lateral shearing for a given ice temperature.

Our coupled model allows us to constrain the mechanisms of ice deformation in natural glacier ice and to estimate the viscous properties of ice for the full range of temperatures and stresses found in glaciers and ice sheets on Earth. We then solve for stress from $\dot{\epsilon}$, d, T using an iterative nonlinear equation solver on Eq. **3**.

2. Deformation Maps: *n* and *A* for Varying Temperatures and Stresses

We estimate Glen's flow law parameters, n and A, for varying stresses and temperatures (and thus, strain rates), and organize the results into deformation maps (Fig. 2). As shown in these maps, dislocation creep ($n = 4$) dominates when stresses are above 100 kPa, while grain boundary sliding ($n = 1.8$) dominates at lower stresses (<10 kPa), as expected from previous studies (14, 15, 38, 56).

At intermediate stresses of order 10 to 100 kPa, a range that describes many regions in fast-flowing areas of Antarctica, the dominant creep mechanism depends strongly on temperature. For both low and high temperatures, grain-boundary sliding ($n = 1.8$) dominates below ~50 kPa. Between 50 and 100 kPa, there is a region of intermediate values $1.8 \leq n \leq 4$. Notably, the region where both dislocation creep and grain-boundary sliding provide controls on flow ($n \sim 3$) is a narrow region in stress-space for a given temperature, suggesting that in most flow regimes, one deformation mechanism tends to dominate over the other. This has implications for ice sheet modeling, as $n = 3$, representing both deformation mechanisms acting as controls on flow, is the commonly used value for the stress exponent in current ice sheet models. Furthermore, the transition between grain-boundary sliding-dominated flow to dislocation creep-dominated flow occurs at a higher stress for lower temperatures ($T < 255$ K) than it does for high temperatures ($T > 260$ K). Thus, dislocation creep controls flow for a greater range of stresses at high temperatures than at lower temperatures.

For $255 \leq T \leq 260$ K, dislocation creep dominates ($n = 4$) for stresses above 10 kPa. This "dip" in the dominance of dislocation creep occurs due to the shifts in activation energy for creep. At $T = 255$ K, there is a sharp increase in activation energy for grain-boundary sliding, thus promoting the effects of dislocation creep since the activation energy for dislocation creep remains low at 255 K. At $T = 258$ K, the activation energy for dislocation creep increases abruptly, transitioning the flow to grain-boundary sliding-dominated flow.

At stresses below 30 kPa and temperatures colder than 255 K, the estimated value of n is anomalously large ($n \sim 2.5$). This is due to elevated grain sizes; at such low temperatures and stresses, normal grain growth, a recrystallization mechanism that operates in regions of low deformation, causes grain size to grow. We do not expect results in these stress-temperature conditions to be realistic nor to impact the primary conclusions of this study because at such low stresses and temperatures, other deformation mechanisms (such as basal slip or diffusion creep) that are not represented in our model may play important roles.

There are a number of uncertainties underlying this model that may affect these estimates of n, including the choice of model for grain size, the values of n_{dis} and n_{gbs}, and the parameters within A_{dis} and A_{gbs} (the prefactor A_{0_i} and the activation energy Q_i for each mechanism $i = \mathrm{dis, gbs}$). The values of n_{i} determine the specific values for grain-boundary sliding-dominated creep and dislocation creep-dominated creep but otherwise do not significantly affect the structure of the

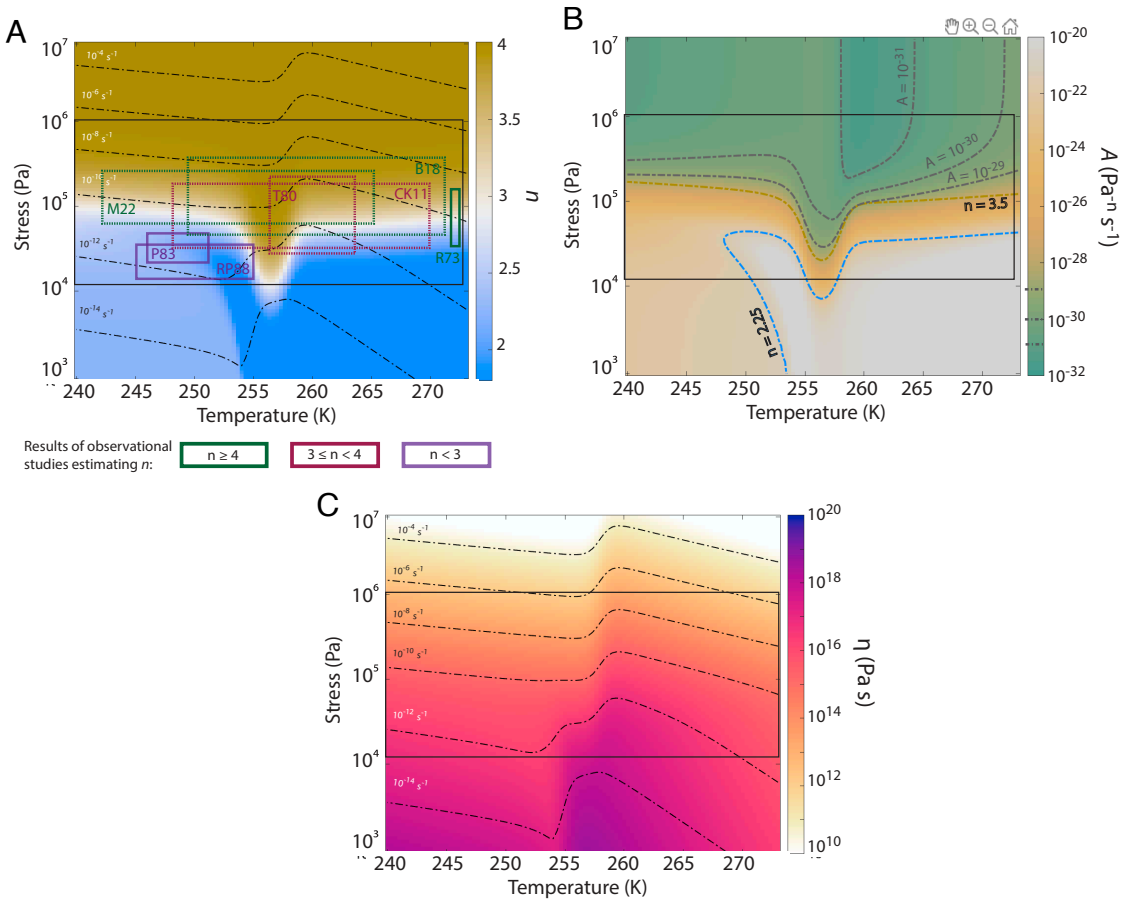

Fig. 2. Estimating n, A, and dynamic viscosity for varying stresses and ice temperatures common in naturally deforming glacier ice. (*A*) Stress exponent in Glen's flow law n from our model compared to multiple observational studies (each shown as a box overlaid on the estimates of n). The colors of the boxes denote the estimated value of n in the observational study. The lines of the box denote confidence in the stress and temperature ranges (solid outlines—explicit ranges of stress and temperature were given in the original study; dashed outlines—ranges were inferred by us based on information provided in the original study and knowledge of regions). The labels, which represent authors' last name and year of publication, and inferred n values are R73 (68) $n = 4.2$, P83 (25) $n = 2.5$ to 3, RP88 (65) $n = 2.9$, T80 (67) ($n = 3$ to 4), and CK11 (66) $n = 3$ to 4. Contour lines show values of constant strain rate. (*B*) The flow-rate parameter in Glen's flow law A from Eq. **2** and assuming isotropic ice viscosity. Contour lines show values of $n = 2.25$ in blue, $n = 3.5$ in gold, and values of A in gray. (*C*) Dynamic viscosity $\eta = \tau^{1-n}/(2A)$. Contour lines show values of constant strain rates.

deformation map. Collectively, the prefactors A_{0_i}, the activation energies Q_i, and the grain sizes determine the stress at which the transition from grain-boundary sliding-dominated flow to dislocation creep-dominated flow occurs. Smaller grain sizes produce grain-boundary sliding-dominated flow at higher stresses than that for larger grain sizes (*SI Appendix*, Fig. S3). This is due to the grain size dependence of grain-boundary sliding in Eq. **3**, in which the rate of grain-boundary sliding is inversely proportional to grain size.

The value of n responds strongly to the activation energies (*SI Appendix*, Fig. S2). The choice of activation energy values at low and high temperatures for grain-boundary sliding and dislocation creep largely control the stress at which the flow transitions from grain-boundary sliding-dominated flow to dislocation creep-dominated flow (and therefore the stress for which $n = 3$ is most applicable for a given temperature). For example, decreasing the activation energy for dislocation creep and increasing the activation energy for grain-boundary sliding would reduce the stress at which this transition occurs. A number of laboratory experiments have estimated these activation energy values for low temperatures, such as refs. 10, 15, 17, and 57–59. Laboratory studies (e.g. refs. 9 and 15) find estimates of activation energy at high temperatures as well, though there have been fewer investigations of this. Further, some evidence suggests that activation energy continues to change as a function of temperature as ice approaches its melting point (8, 20, 45), while currently it is treated as constant above the transition temperature. These results point to a need for further investigation of activation energy particularly at high temperatures to reduce uncertainties in the deformation of ice and the value of n. This is further explored in *SI Appendix*.

Changing the prefactors A_{0_i} within approximately an order of magnitude produces less change in the deformation mechanism map than changing activation energies (*SI Appendix*, Fig. S1). This is especially relevant because the prefactors A_{0_i} are most likely to change due to microstructural evolution, such as fabric development, and such development produces at most an order of magnitude change in the prefactor (60–64). This would imply that physical processes that can be parameterized as a multiplicative enhancement factor on A have less of an effect on estimates of n than uncertainties in activation energies or grain size estimates.

This model can provide insight into the variations in observational studies from $n \approx 2$ to 4 as a manifestation of measurements being taken at various stresses and ice temperatures (Fig. 2*A*). We highlight the results of a selection of observational studies with

boxes in Fig. 2*A*. Many of the studies concluding $n = 2$ to 3 have been done in conditions that fall below the boundary between $n = 1.8$ and 4, with stresses of 10 to 100 kPa and temperatures <255 K (e.g., ref. 25 in Byrd Station, Antarctica and Camp Century, Greenland and ref. 65 in Devon Island Ice Cap, Canada). Studies on Taylor Glacier, Antarctica (66), and Roosevelt Island, Antarctica (67), conclude that n may vary between $n = 3$ and 4. These two studies considered slightly higher stresses and a wider range of ice temperatures, falling between the boundary of $n = 3$ and 4 in our deformation map. Finally, studies across the upper region of the GrIS (29) and on Antarctic ice shelves (30) estimate values of $n \geq 4$ at stresses between approximately 30 to 200 kPa. Neither study provides an estimate of ice temperature, so we take temperature to be uncertain (Fig. 2*A*), making direct comparison more difficult. However, for the given stresses, our model estimates $n \geq 3$ for all temperatures and estimates $n \approx 4$ for most of the stress-temperature space, suggesting reasonable agreement between these studies and our model.

The most significant deviation between observational studies and our model is with the study of Ranganathan et al. (68), which finds an estimate of $n = 4.2$ in Athabasca Glacier, a temperate alpine glacier. Our model estimates a lower value of $n \approx 3$ than is found in observations at the temperatures ($T \approx 273$ K) and stresses of the study region. Some likely causes of this discrepancy, as discussed above, are uncertainty in the estimates for high-temperature activation energy for grain-boundary sliding and dislocation creep, which have only been constrained in a handful of studies, or uncertainties in the grain sizes in temperate glaciers. The latter is especially relevant since the processes governing grain size are not as well constrained in ice at the melting temperature. The model we apply here also does not allow for values of $n > 4$, which may suggest some uncertainty in the stress exponents associated with dislocation creep and grain-boundary sliding.

Applying our estimates of n to Glen's flow law, we calculate the prefactor A for isotropic ice viscosity (Fig. 2*B*). In regions where $n \approx 4$, we estimate $A \leq 10^{-28}$ Pa^{-n} s^{-1}, while where $n \approx 2$, $A > 10^{-22}$ Pa^{-n} s^{-1}. Given the difference in the stress exponent, the increase in the magnitude of A for decreasing n is expected because as the stress exponent decreases, A must increase to produce strain rates that are of a similar order of magnitude.

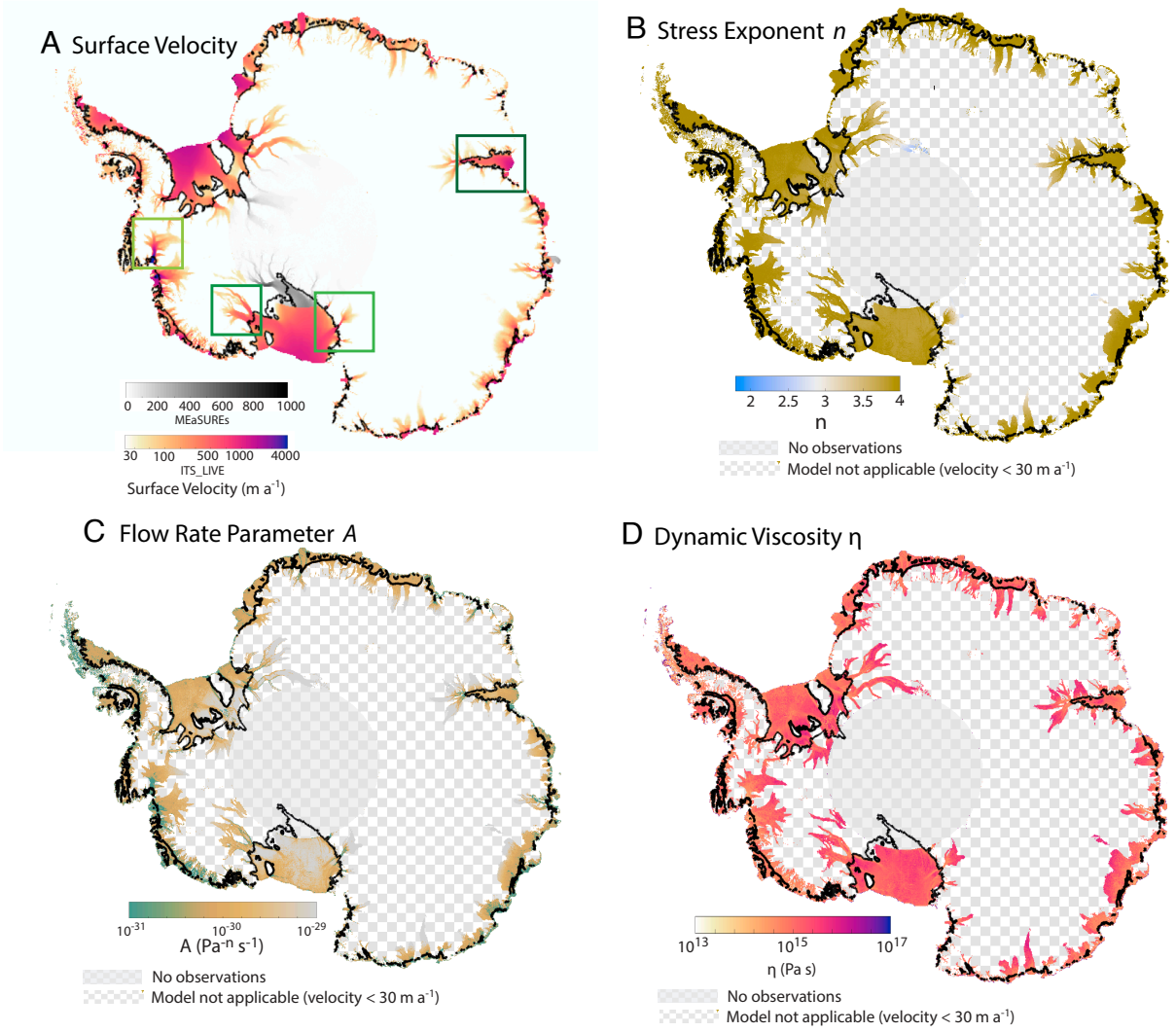

Fig. 3. Estimating n and A across the Antarctic Ice Sheet: using observations of (*A*) surface velocity (3, 4) and (*B*) calculated strain rates (72), we estimate (*C*) n and (*D*) A over the Antarctic Ice Sheet. Dark gray checkered regions show gaps in the data, and light gray checkered regions are where measured ice velocity is less than 30 m a^{-1}, and our model is not applicable because observed surface strain rates do not represent strain rates at depth. Solid lines denote the grounding line from Bedmap2 (73).

With estimates of both n and A, we can estimate dynamic viscosity as $\eta = \tau^{1-n}/(2A)$. Dynamic viscosity varies from 10^{12} to 10^{16} Pa · s for the typical range of stresses in ice sheets and is primarily sensitive to stress over temperature. There are no significant nonlinearities in dynamic viscosity near the transition stress between grain-boundary sliding-dominated flow and dislocation creep-dominated flow. This is because the change in the magnitude of A at that transition offsets this effect, producing a roughly smooth increase in dynamic viscosity with stress.

Using this method and with reasonable estimates of n, strain rate, and applied stress, we can estimate ice viscosity in natural ice sheets, providing insight into the magnitude of ice softening due to mechanisms such as shear heating and recrystallization.

3. Estimates of *n* and *A* in the AIS

Our model demonstrates how fundamental rheological parameters are affected by ice flow conditions, and it enables estimates of the dominant deformation mechanisms and relevant viscous parameters across the AIS. This is possible because ice in Antarctica should be relatively dry; ultimately, we will be able to apply the model to wetter ice in Greenland once we better understand how intergranular liquid water content influences the balance of creep mechanisms. Here, we present estimates in the AIS with specific focus on Pine Island Glacier, Byrd Glacier, Bindschadler and MacAyeal Ice Streams, and Amery Ice Shelf, all of which are well-observed, fast-flowing areas that represent a range of dynamical characteristics. Computing n, A requires observations of effective strain rate, ice thickness, and surface mass balance. Effective strain rates are derived from Landsat 7 and 8 velocity fields (3) using methods described in ref. 46. Ice thickness is calculated from basal topography from BedMachine (69) and surface elevation from the Reference Elevation Model of Antarctica (70). Surface mass balance, averaged over 1979 to 2019, is estimated from the Regional Atmospheric Climate Model (RACMO) (71). The estimates presented here are depth-averaged.

We estimate $n \geq 3.6$ in all fast-flowing areas of the AIS (Figs. 3 and 4). Notably, we estimate very few regions with $n = 3$, the canonical value used in most ice sheet models. Within ice streams, the value of n varies between $n \approx 3.6$ and $n \approx 4$ (Fig. 4). In general, we find $n \approx 4$ in regions of rapid deformation, such as the margins of glaciers, and we find $3.6 \leq n < 4$ in slower-deforming regions, such as in the centerline of the ice shelves. In Pine Island Glacier, our model finds $n = 4$ across the entire glacier, due to the magnitude of strain rates and velocity in Pine Island Glacier. Similarly in Byrd Glacier, we estimate $n = 4$ for all of the grounded regions except the inflow boundary, and we estimate $n = 4$ around the grounding line on the ice shelf. The value of n begins to decay with distance from the grounding line on the ice shelf. Bindschadler and MacAyeal Ice Streams show more variation. On the ice shelf of Bindschadler and MacAyeal Ice Streams, we estimate $n \approx 3.7$, while we estimate $n = 4$ in the grounded part of the ice streams and in the shear margins

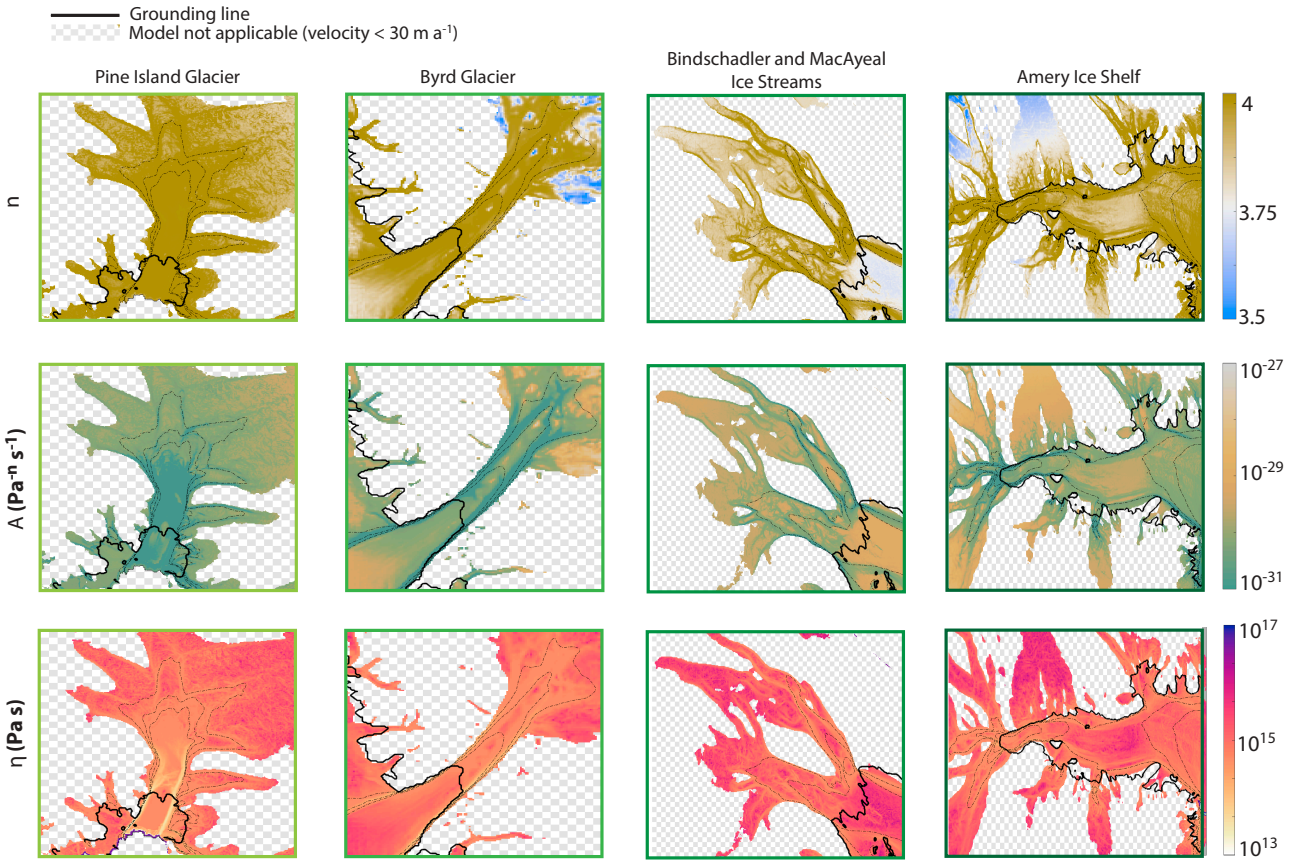

Fig. 4. Estimating n and A in Antarctic ice streams: n (*Upper* row), A (*Middle* row), and dynamic viscosity η (*Lower* row) in (*Left* to *Right*) Pine Island Glacier, Byrd Glacier, Bindschadler and MacAyeal Ice Streams, and the Amery Ice Shelf. Dashed lines denote surface velocity contours of 200 m yr^{-1}, 400 m yr^{-1}, and 600 m yr^{-1}. Solid lines denote the grounding line from Bedmap2 (73). Gray checkered regions are where measured ice velocity is less than 30 m a^{-1}, and our model is not applicable because observed surface strain rates do not represent strain rates at depth.

on the ice shelf. Finally, we estimate $n = 4$ across Amery Ice Shelf, with a region of slightly lower values in the center of the ice shelf.

We find slightly lower estimates in the center of the Ross Ice Shelf than is found by Millstein et al. (30), which applied observations of surface strain rates and ice thickness to estimate the stress exponent n. Millstein et al. (30) estimated $n \geq 4$ across the ice shelf, with estimates ranging from $n = 3.9$ to 4.5. In the same areas, we find $n \approx 3.75$. As discussed in the previous section, this could be due to parametric uncertainties, such as activation energy. In particular, underestimating the activation energy for grain boundary sliding and/or overestimating the activation energy for dislocation creep would produce lower estimates of n. Another likely cause is the choice of temperature and grain-size models. In particular, the ice temperature model is a one-dimensional model that neglects effects of along-flow and lateral advection of ice and assumes that ice temperature is in steady state. Similarly, the grain-size model is also one-dimensional and assumes steady-state. While in general, these are good assumptions for fast-flowing areas, these assumptions could produce small deviations from observations in the model estimates. A useful direction for future work would be to incorporate more complex temperature and grain-size models, which would also allow us to apply these estimates to slower-flowing regions (checkered regions of Fig. 3).

Our results here are also not inconsistent with the results of Behn et al. (32). They find that $n = 3$ by coupling the composite flow law used in this study (15) to a grain-size model derived from ref. 74. We similarly find $n = 3$ to be valid for a range of stresses and temperatures (Fig. 2*A*), though we estimate larger n values for faster deforming regions. A key distinction between their estimates and the ones presented in this study is in the grain size model. We apply a grain-size model that accounts for different recrystallization mechanisms (47), producing coarser grain estimates than that of Behn et al. (32). This results in larger estimates of n. However, the framework and underlying physics explored in this study are consistent with that of Behn et al. (32), and their study similarly finds the importance of understanding grain size evolution in order to represent ice deformation in models.

We also present estimates of the flow-rate parameter A across the AIS and in specific regions of the ice sheet (Fig. 3). The variations in A are primarily the result of variations in n, since A varies orders of magnitude in response to changes in n. For example, in Bindschadler and MacAyeal Ice Streams, we estimate $A \approx 10^{-31}$ Pa^{-n} s^{-1} in the margins of the grounded region, while A is approximately two orders of magnitude larger in the center of the ice shelf. This is likely because n is larger in the margins of the grounded region.

To visualize regions of ice softening, we estimate dynamic viscosity η, which is a function of both A and n, and thus changes in dynamic viscosity are a result of physical processes softening ice rather than calibration due to different parameter values. In Antarctic ice streams, lateral shear is primarily localized in the lateral margins, and thus in our model, the margins of ice streams are warmer and expected to have larger grain sizes than the center regions of the ice stream (47). Both of these processes affect estimates of ice viscosity. Here, we see generally that η is lower in these rapidly deforming regions of the ice sheet. This is especially evident in the margins of Pine Island Glacier, where dynamic viscosity is approximately 1.5 orders of magnitude lower than it is in the centerline. This result is in line with a number of modeling and computational studies suggesting that ice is warmer and softer in shear margins (52, 75–79). We also expect strong (likely close to single maximum) fabric in lateral shear margins (60, 62, 63), which can decrease dynamic viscosity by an order of magnitude.

4. Discussion and Conclusion

How we model ice deformation has significant effects on glacier dynamics, projections of glacier behavior, ice-sheet stability, and sea-level rise (Fig. 1). Our model provides physically informed estimates of the fundamental parameters underlying our representation of viscous ice flow: the stress exponent n and prefactor A in Glen's flow law. The practical implications of our model are 1) a physical basis for scaling from laboratory ice to natural glacier ice, 2) the unification of ice deformation that captures and contextualizes the range of existing estimates of the stress exponent n, and 3) the establishment of a framework for estimating the values of A and n in Glen's flow law (Eq. **2**) based on first principles, laboratory experiments, and observations. This modeling framework can be readily applied to existing ice-flow models while respecting the various coupled physical processes, such as internal heating due to deformation and evolving grain sizes, as a way of improving our parameterization of ice deformation and as part of a broader community effort to make more reliable projections of sea-level rise.

Our results further depend on some key assumptions about ice flow. Importantly, they depend on the assumption that dislocation creep and grain-boundary sliding are both active in ice sheets, that the contributions of these two mechanisms operate independently such that their contributions can be summed according to the composite flow law (Eq. **1**), and that they are the dominant two mechanisms controlling ice flow in natural conditions. Some studies have suggested that the behavior identified by Goldsby and Kohlstedt (15, 38) as grain-boundary sliding may in fact be descriptive of other processes, such as the accommodation of basal slip by grain-boundary migration, which acts as a recovery mechanism (40, 80). While more work needs to be done to determine the physical mechanism behind the $n = 1.8$ regime, the analysis here should be robust to the specific mechanisms that produce the stress dependencies, since this work is interested primarily in determining under which conditions each regime is most applicable. However, uncertainties would be reduced by further investigation into which process is dominant and the incorporation of a physical understanding of that process into the model.

Relatedly, these results are further dependent upon the construction of the composite flow law itself, as presented in ref. 15. Multiterm flow laws have been presented in a number of studies to describe changes in flow mechanisms at varying stresses. These flow laws are all similar in that they are generally constructed such that a term with a lower stress exponent dominates at lower stresses and a term with a higher stress exponent dominates at higher stresses, in agreement with observational and laboratory data (13, 81–83). Many of these multiterm flow laws are empirical or phenomenological, setting up terms that do not explicitly describe physical mechanisms but rather are used to describe a changing nonlinearity of flow with stress (56, 82, 84, 85). Many of these multiterm flow laws have either two or three terms. Those with two terms generally have a linear term and a term with $n = 3$, as in ref. 56. Those with three terms typically have terms with $n = 1$, 3, and 5, as in refs. 82 and 85. While here we use the composite flow law presented in ref. 15, for future work, other multiterm flow laws could be used

in this framework presented in this study to evaluate the range of n estimates for varying flow laws.

Other processes not considered here include the effect of anisotropy (fabric). Fabric may increase the rate of ice deformation up to an order of magnitude, due to the development of a crystallographic preferred orientation from rotation caused by basal slip (60, 62, 86–88). Many modeling frameworks suggest that fabric can be parameterized by a strain rate enhancement factor of ~2 to 10 (60, 61, 63, 89). As demonstrated in *SI Appendix*, Fig. S1, effects of processes, such as fabric, that can be represented as multiplicative enhancement factors are likely to affect dynamic viscosity through enhancement to the flow-rate parameter A but are only likely to affect estimates of n if fabric affects dislocation creep and grain-boundary sliding differently. Therefore, understanding the effects of processes such as fabric on different deformation mechanisms individually is an important step for future work.

Because we focus on the stresses and temperatures found in existing glaciers and ice sheets, this work does not account for other creep mechanisms such as diffusion creep and basal-slip accommodated grain-boundary sliding (Eq. **3**). While Goldsby and Kohlstedt (15) suggest that mechanisms like diffusion creep and basal slip are unlikely to be dominant in rapidly deforming ice, these regimes should be considered when extending this work to slower-flowing regions of ice sheets, such as flow near ice divides.

While we neglect some of the complexity of ice flow, we believe this study is a step toward understanding the controls of ice flow and identifying the parameters in ice flow models that ought to be further constrained. Additional complexities in the deformation of ice could be incorporated into this framework by altering the composite flow law used.

We provide a framework for modeling the variability of the viscous flow parameters with realistic stress and temperature conditions, which provides a step toward incorporating increased physical complexity into ice flow models with minimal increases in the complexity of the models themselves. Interested readers will find the results shown in the deformation maps (Fig. 2) in an hdf5 file in *SI Appendix*, which can be used as a simple look-up table in ice-flow models and those used for sea-level rise projections. Such a framework should bolster the physical underpinnings of models used to study glacier dynamics and project sea level and to understand more broadly how glaciers and ice sheets evolve with climate.

5. Materials and Methods

To estimate the viscous stress exponent n and prefactor A, we couple the composite flow law presented in ref. 15 with a model for ice temperature (46) and a model for steady-state grain size (47). The composite flow law explicitly represents multiple ice deformation mechanisms and is dependent upon the applied stress, the ice temperature, and the grain size, along with kinetic parameters (such as the activation energy and prefactor in the Arrhenius relation). Below, we discuss the models and relevant calculations.

5.1. Models for Estimating Rheology Parameters. The coupled model makes a few key assumptions. In estimating ice temperature and grain size, we first assume that both temperature and grain-size are in steady state, a justified assumption based on the timescales to steady-state, as shown in ref. 47. Therefore, the results shown here can be interpreted as constraining the mechanisms by which ice flows assuming a steady or slowly varying forcing. Second, the ice temperature and grain size models assume that the only advection of ice occurs vertically, and therefore horizontal (lateral and along-flow) advection is negligible.

Table 2. Parameters used in the ice temperature model

Parameter	Value	Unit
ρ	917	kg m^{-3}
c_p	2,050	J kg^{-1} K^{-1}
a	60 or found from data	mm y^{-1}
T_m	273	K
K	2.1	W m^{-1} K^{-1}

5.1.1. Ice temperature model. To find ice temperature, we apply a one-dimensional thermomechanical model derived in ref. 46. This model represents vertical advection and diffusion of heat as well as a shear heating term. The shear heating term describes the irreversible dissipation of heat due to viscous deformation. Ice temperature is found by solving the following equation:

$$-\rho c_p a \frac{\partial T}{\partial z} = K \frac{\partial^2 T}{\partial z^2} + \tau_{ij}\dot{\epsilon}_{ij}, \quad [5]$$

where ρ is the mass density of ice, c_p is the specific heat capacity of ice, a is ice accumulation, T is ice temperature, z is the vertical coordinate (defined as being positive upward and parallel to the gravity vector), K is thermal conductivity, τ_{ij} is the deviatoric stress tensor (we assume ice is incompressible), and $\dot{\epsilon}_{ij}$ is the strain rate tensor. This equation is solved with the boundary conditions of $T = T_m$ at the boundary between cold and temperate ice, where T_m is the melting temperature, $T = T_s$ at the surface of the ice, where T_s is the surface temperature, and $-K\frac{\partial T}{\partial z} = 0$ at the cold-temperate boundary. The parameters used are found in Table 2 and the analytical solution to Eq. **5** can be found in ref. 46 along with further details on the model.

5.1.2. Grain size model. To find grain size, we apply a one-dimensional steady-state grain size model derived in ref. 47. This model computes the changes in grain size that occur due to recrystallization, a class of mechanisms that alter the size, shape, and orientation of ice grains. The model represents three mechanisms: normal grain growth, which grows grains in the absence of deformation to reduce surface energy (90), rotation recrystallization, which reduces grains in the presence of low-temperature deformation to reduce elastic strain energy (91), and migration recrystallization, which increases grain size in the presence of high-temperature deformation to reduce elastic strain energy (11, 91). Steady-state grain size is then found through the balances in surface and strain energies (47, 74) as

$$d = \left[\frac{4kp^{-1}c\gamma\mu^2 + \tau^4 D^p (\frac{p}{2}) M}{8(1-\Theta)\tau\dot{\epsilon}\mu^2}\right]^{\frac{1}{1+p}}, \quad [6]$$

Table 3. Parameters used in the grain size model

Parameter	Value	Unit
k	$k_0 \exp\left\{-\frac{Q_{gg}}{RT}\right\}$	mm^p s^{-1}
k_0	11.4266	mm^p s^{-1}
Q_{gg}^-	40	kJ mol^{-1}
Q_{gg}^+	100	kJ mol^{-1}
p	9	–
c	6	–
γ	0.065	J m^{-2}
μ	3×10^9	Pa
D	0.3	m
M	$M_0 \exp\left\{-\frac{Q_m}{RT}\right\}$	m^2 s kg^{-1}
M_0	0.023	m^2 s kg^{-1}
Q_m^-	100	kJ mol^{-1}
Q_m^+	40	kJ mol^{-1}
Θ	0.99	–

Low temperatures are those below 263 K and labeled with superscript$^-$, while high temperatures are above 263 K and labeled with superscript$^+$.

where k is the normal grain growth rate factor, p is the grain growth exponent, c represents the shape of grains, γ is grain boundary energy, μ is the shear modulus of ice, D is the characteristic length scale for strain energy, M is grain boundary mobility, and Θ is the partitioning between stored and thermal energy when ice deforms. The parameters we use are given in Table 3 and discussed in detail in ref. 47.

5.2. Updated Flow Law for Use in Ice-Flow Models. To simplify the incorporation of our updated flow law, we provide readers with the option to query our model results for values of n, A, and dynamic viscosity ($\eta = \tau^{1-n}/(2A)$) appropriate to their modeling needs. The results presented in the deformation maps of Fig. 2 in the main text are provided as an hdf5 file in *SI Appendix* and on Zenodo. Users may prefer to fit a spline to this surface for easy incorporation into their models.

5.3. Glacier Stability Model. To demonstrate the effect of n and A on marine ice sheet stability, we apply a model derived by ref. 35, which builds on work by ref. 34. This model estimates steady-state grounding line positions to analyze the stability of ice sheets. The glacier is laterally confined, with prescribed width $W = 40$ km and length of the ice shelf $L_s = 115$ km. The bed is defined as in ref. 35, and a portion of the bed has a retrograde slope. Assuming a constant temperature of $T = 270$ K and grain size of 1 mm in all three cases, we estimate the steady-state grounding line flux q in the limit of strong buttressing (when $W \ll L_s$; (35), equation 22a):

$$q = \frac{[\rho_i g(1-\rho_i/\rho_w)]^n A W^{n+1}}{(4^n C_w)^{1/(n+1)} W + \frac{1+n}{n} C_w L_s} h_g^{n+1}, \qquad [7]$$

where ρ_i is the density of ice, ρ_w is the density of water, C_w is a parameter describing lateral shear stress, h_g is the ice thickness at the grounding line. The values of the parameters used are the same as described in ref. 35. To find steady states, Eq. **7** must equal the total mass accumulation ax_g, where a represents the rate of snow accumulation. The grounding line flux intersects with the mass accumulation integrated over the grounded portion of the ice stream at the steady-state grounding line positions.

Data, Materials, and Software Availability. The source code for the model presented in this study are openly available at: https://github.com/megr090/DeformationMechanisms. No new data were produced for this study, and data used in this study are publicly available through their respective publications (69–71, 73).

ACKNOWLEDGMENTS. We thank two anonymous reviewers and the scientific editor for their time and valuable feedback. We benefited greatly from discussions with Joanna Millstein, David Goldsby, Mark Behn, Colin R. Meyer, and Jerome Neufeld. We thank Marianne Haseloff for providing the code for the ice sheet stability model, and for providing the information for running the model. M.R. was supported by the School of Science Service Fellowship, the Martin Fellowship, National Science Foundation Directorate for Geosciences and the Natural Environment Research Council (NSFGEO-NERC) award 1853918 and the Nippon Electric Company (NEC) Corporation Fund for Research in Computers and Communications. B.M. acknowledges funding from NSFGEO-NERC award 1853918, NSF-NERC award 1739031, and the NEC Corporation Fund for Research in Computers and Communications.

1. B. Fox-Kemper *et al.*, *Cryosphere and Sea Level Change in Climate Change 2021–The Physical Science Basis: Working Group I Contribution to the Sixth Assessment Report of the Intergovernmental Panel on Climate Change* (Cambridge University Press, ed. 1, 2021).
2. E. Rignot, J. Mouginot, B. Scheuchl, Ice flow of the Antarctic ice sheet. *Science* **333**, 1427–1430 (2011).
3. A. S. Gardner *et al.*, Increased West Antarctic and unchanged East Antarctic ice discharge over the last 7 years. *Cryosphere* **12**, 521–547 (2018).
4. J. Mouginot, E. Rignot, B. Scheuchl, Continent-wide, interferometric SAR phase, mapping of Antarctic ice velocity. *Geophys. Res. Lett.* **46**, 9710–9718 (2019).
5. J. De Rydt, R. Reese, F. S. Paolo, G. H. Gudmundsson, Drivers of Pine Island Glacier speed-up between 1996 and 2016. *Cryosphere* **15**, 113–132 (2021).
6. K. M. Cuffey, "Manifestations of ice microphysical processes at the scale of whole ice sheets" in *Glacier Science and Environmental Change*, P. G. Knight, Ed. (Blackwell Publishing, Malden, MA, 2006), pp. 290–300.
7. D. J. Bromer, W. D. Kingery, Flow of polycrystalline ice at low stresses and small strains. *J. Appl. Phys.* **39**, 1688–1691 (1968).
8. M. Mellor, R. Testa, Creep of ice under low stress. *J. Glaciol.* **8**, 147–152 (1969).
9. P. Barnes, D. Tabor, J. Walker, The friction and creep of polycrystalline ice. *Proc. R. Soc. A, Math. Phys. Eng. Sci.* **324**, 127–155 (1971).
10. P. Duval, H. Le Gac, Mechanical behaviour of Antarctic ice. *Ann. Glaciol.* **3**, 92–95 (1982).
11. P. Duval, M. F. Ashby, I. Anderman, Rate-controlling processes in the creep of polycrystalline ice. *J. Phys. Chem.* **87**, 4066–4074 (1983).
12. M. Montagnat, P. Duval, Rate controlling processes in the creep of Polar ice, influence of grain boundary migration associated with recrystallization. *Earth Planet. Sci. Lett.* **183**, 179–186 (2000).
13. W. B. Durham, L. A. Stern, S. H. Kirby, Rheology of ice I at low stress and elevated confining pressure. *J. Geophys. Res. Solid Earth* **106**, 11031–11042 (2001).
14. D. Goldsby, D. Kohlstedt, Grain boundary sliding in fine-grained Ice I. *Scr. Mater.* **37**, 1399–1406 (1997).
15. D. L. Goldsby, D. L. Kohlstedt, Superplastic deformation of ice: Experimental observations. *J. Geophys. Res. Solid Earth* **106**, 11017–11030 (2001).
16. W. Durham, L. Stern, Rheological properties of water ice-applications to satellites of the outer planets. *Annu. Rev. Earth Planet. Sci.* **29**, 295–330 (2001).
17. J. Glen, The creep of polycrystalline ice. *Proc. R. Soc. A, Math. Phys. Eng. Sci.* **228**, 519–538 (1955).
18. R. H. Thomas, The creep of ice shelves: Interpretation of observed behaviour. *J. Glaciol.* **12**, 55–70 (1973).
19. K. C. Jezek, R. B. Alley, R. H. Thomas, Rheology of glacier ice. *Science* **227**, 1335–1337 (1985).
20. W. Budd, T. Jacka, A review of ice rheology for ice sheet modelling. *Cold Reg. Sci. Technol.* **16**, 107–144 (1989).
21. E. Larour, Rheology of the Ronne Ice Shelf, Antarctica, inferred from satellite radar interferometry data using an inverse control method. *Geophys. Res. Lett.* **32**, L05503 (2005).
22. K. Cuffey, W. Paterson, *The Physics of Glaciers* (Elsevier Inc., ed. 4, 2010).
23. B. Riel, B. Minchew, Variational inference of ice shelf rheology with physics-informed machine learning. *J. Glaciol.* **69**, 1–20 (2023).
24. P. J. Martin, T. J. O. Sanderson, Morphology and dynamics of ice rises. *J. Glaciol.* **25**, 33–46 (1980).
25. W. Paterson, Deformation within Polar ice sheets: An analysis of the Byrd station and camp century borehole-tilting measurements. *Cold Reg. Sci. Technol.* **8**, 165–179 (1983).
26. C. J. C. Adams, N. R. Iverson, C. Helanow, L. K. Zoet, C. E. Bate, Softening of temperate ice by interstitial water. *Front. Earth Sci.* **9**, 702761 (2021).
27. J. Nye, The distribution of stress and velocity in glaciers and ice-sheets. *Proc. R. Soc. London Ser. A, Math. Phys. Sci.* **239**, 113–133 (1957).
28. F. Gillet-Chaulet, R. C. A. Hindmarsh, H. F. J. Corr, E. C. King, A. Jenkins, In-situ quantification of ice rheology and direct measurement of the Raymond Effect at Summit, Greenland using a phase-sensitive radar. *Geophys. Res. Lett.* **38**, 1480 (2011).
29. P. D. Bons *et al.*, Greenland ice sheet: Higher nonlinearity of ice flow significantly reduces estimated basal motion. *Geophys. Res. Lett.* **45**, 6542–6548 (2018).
30. J. D. Millstein, B. M. Minchew, S. S. Pegler, Ice viscosity is more sensitive to stress than commonly assumed. *Commun. Earth Environ.* **3**, 57 (2022).
31. V. Rommelaere, D. R. MacAyeal, Large-scale rheology of the Ross Ice Shelf, Antarctica, computed by a control method. *Ann. Glaciol.* **24**, 43–48 (1997).
32. M. D. Behn, D. L. Goldsby, G. Hirth, The role of grain size evolution in the rheology of ice: Implications for reconciling laboratory creep data and the Glen flow law. *Cryosphere* **15**, 4589–4605 (2021).
33. M. Zeitz, A. Levermann, R. Winkelmann, Sensitivity of ice loss to uncertainty in flow law parameters in an idealized one-dimensional geometry. *Cryosphere* **14**, 3537–3550 (2020).
34. C. Schoof, Ice sheet grounding line dynamics: Steady states, stability, and hysteresis. *J. Geophys. Res.* **112**, F03S28 (2007).
35. M. Haseloff, O. V. Sergienko, Effects of calving and submarine melting on steady states and stability of buttressed marine ice sheets. *J. Glaciol.* **68**, 1149–1166 (2022).
36. J. Weertman, Stability of the junction of an ice sheet and an ice shelf. *J. Glaciol.* **13**, 3–11 (1974).
37. I. Joughin, B. E. Smith, B. Medley, Marine ice sheet collapse potentially under way for the Thwaites Glacier Basin, West Antarctica. *Science* **344**, 735–738 (2014).
38. D. L. Goldsby, D. L. Kohlstedt, Flow of ice I by dislocation, grain boundary sliding, and diffusion processes. *Lunar Planet. Sci.* **28**, 429–430 (1997).
39. P. Pimienta, P. Duval, V. Y. Lipenkov, "Mechanical behavior of anisotropic Polar ice" in *The Physical Basis of Ice Sheet Modelling*, E. D. Waddington, J. S. Walder, Eds. (IAHS, 1987), vol. 170.
40. P. Duval, M. Montagnat, Comment on "Superplastic deformation of ice: Experimental observations" by D. L. Goldsby and D. L. Kohlstedt. *J. Geophys. Res. Solid Earth* **107**, ECV 4-1–ECV 4-2 (2002).
41. M. Ashby, A first report on deformation-mechanism maps. *Acta Metall.* **20**, 887–897 (1972).
42. H. Frost, M. Ashby, *Deformation-Mechanism Maps: The Plasticity and Creep of Metals and Ceramics* (Pergamon Press Ltd., 1982).
43. J. Poirier, *Creep of Crystals: High-Temperature Deformation Processes in Metals, Ceramics, and Minerals* (Cambridge University Press, 1985).
44. M. Ohtomo, G. Wakahama, Growth rate of recrystallization in ice. *J. Phys. Chem.* **87**, 4139–4142 (1983).
45. T. Jacka, L. Jun, The steady-state crystal size of deforming ice. *Ann. Glaciol.* **20**, 13–18 (1994).
46. C. R. Meyer, B. M. Minchew, Temperate ice in the shear margins of the Antarctic ice sheet: Controlling processes and preliminary locations. *Earth Planet. Sci. Lett.* **498**, 17–26 (2018).
47. M. Ranganathan, B. Minchew, C. R. Meyer, M. Peč, Recrystallization of ice enhances the creep and vulnerability to fracture of ice shelves. *Earth Planet. Sci. Lett.* **576**, 117219 (2021).
48. P. Duval, Grain growth and mechanical behaviour of Polar ice. *Ann. Glaciol.* **6**, 79–82 (1985).
49. R. B. Alley, Fabrics in Polar ice sheets: Development and prediction. *Science* **240**, 493–495 (1988).
50. J. G. Dash, A. W. Rempel, J. S. Wettlaufer, The physics of premelted ice and its geophysical consequences. *Rev. Mod. Phys.* **78**, 695–741 (2006).
51. M. Ranganathan, B. Minchew, C. R. Meyer, G. H. Gudmundsson, A new approach to inferring basal drag and ice rheology in ice streams, with applications to West Antarctic ice streams. *J. Glaciol.* **67**, 229–242 (2021).

52. M. Ranganathan, J. W. Barotta, C. R. Meyer, B. Minchew, Meltwater generation in ice stream shear margins: Case study in Antarctic ice streams. *Proc. R. Soc. A, Math. Phys. Eng. Sci.* **479** (2023).
53. D. R. MacAyeal, R. A. Bindschadler, T. A. Scambos, Basal friction of ice stream E, West Antarctica. *J. Glaciol.* **41**, 247–262 (1995).
54. I. Joughin, D. R. MacAyeal, S. Tulaczyk, Basal shear stress of the Ross ice streams from control method inversions: Shear stress of the Ross ice streams. *J. Geophys. Res. Solid Earth* **109**, B09405 (2004).
55. M. Morlighem, H. Seroussi, E. Larour, E. Rignot, Inversion of basal friction in Antarctica using exact and incomplete adjoints of a higher-order model. *J. Geophys. Res. Earth Surface* **118**, 1746–1753 (2013).
56. E. C. Pettit, E. D. Waddington, Ice flow at low deviatoric stress. *J. Glaciol.* **49**, 359–369 (2003).
57. W. S. B. Paterson, Secondary and tertiary creep of glacier ice as measured by borehole closure rates. *Rev. Geophys.* **15**, 47 (1977).
58. J. Weertman, Creep deformation of ice. *Annu. Rev. Earth Planet. Sci.* **11**, 215–240 (1983).
59. S. Fan *et al*., Temperature and strain controls on ice deformation mechanisms: Insights from the microstructures of samples deformed to progressively higher strains at 10, 20, and 30°C. *Cryosphere* **14**, 3875–3905 (2020).
60. Y. Ma *et al*., Enhancement factors for grounded ice and ice shelves inferred from an anisotropic ice-flow model. *J. Glaciol.* **56**, 805–812 (2010).
61. B. M. Minchew, C. R. Meyer, A. A. Robel, G. H. Gudmundsson, M. Simons, Processes controlling the downstream evolution of ice rheology in glacier shear margins: Case study on Rutford ice stream, West Antarctica. *J. Glaciol.* **64**, 583–594 (2018).
62. D. A. Lilien, N. M. Rathmann, C. S. Hvidberg, D. Dahl-Jensen, Modeling ice-crystal fabric as a proxy for ice-stream stability. *J. Geophys. Res. Earth Surface* **126**, e2021JF006306 (2021).
63. N. M. Rathmann, C. S. Hvidberg, A. Grinsted, D. A. Lilien, D. Dahl-Jensen, Effect of an orientation-dependent non-linear grain fluidity on bulk directional enhancement factors. *J. Glaciol.* **67**, 569–575 (2021).
64. T. A. Gerber *et al*., Crystal orientation fabric anisotropy causes directional hardening of the Northeast Greenland ice stream. *Nat. Commun.* **14**, 2653 (2023).
65. N. Reeh, W. Paterson, Application of a flow model to the ice-divide region of Devon Island ice cap, Canada. *J. Glaciol.* **34**, 55–63 (1988).
66. K. Cuffey, J. Kavanaugh, How nonlinear is the creep deformation of Polar ice? A new field assessment. *Geology* **39**, 1027–1030 (2011).
67. R. H. Thomas, D. R. MacAyeal, C. R. Bentley, J. L. Clapp, The creep of ice, geothermal heat flow, and Roosevelt Island, Antarctica. *J. Glaciol.* **25**, 47–60 (1980).
68. C. F. Raymond, Inversion of flow measurements for stress and rheological parameters in a Valley Glacier. *J. Glaciol.* **12**, 19–44 (1973).
69. M. Morlighem *et al*., Deep glacial troughs and stabilizing ridges unveiled beneath the margins of the Antarctic ice sheet. *Nat. Geosci.* **13**, 132–137 (2020).
70. I. M. Howat, C. Porter, B. E. Smith, M. J. Noh, P. Morin, The reference elevation model of Antarctica. *Cryosphere* **13**, 665–674 (2019).
71. J. Van Wessem *et al*., Improved representation of East Antarctic surface mass balance in a regional atmospheric climate model. *J. Glaciol.* **60**, 761–770 (2014).
72. B. M. Minchew, M. Simons, B. Riel, P. Milillo, Tidally induced variations in vertical and horizontal motion on Rutford ice stream, West Antarctica, inferred from remotely sensed observations. *J. Geophys. Res. Earth Surface* **122**, 167–190 (2017).
73. P. Fretwell *et al*., Bedmap2: Improved ice bed, surface and thickness datasets for Antarctica. *Cryosphere* **7**, 375–393 (2013).
74. N. J. Austin, B. Evans, Paleowattmeters: A scaling relation for dynamically recrystallized grain size. *Geology* **35**, 343 (2007).
75. H. P. Jacobson, C. F. Raymond, Thermal effects on the location of ice stream margins. *J. Geophys. Res. Solid Earth* **103**, 12111–12122 (1998).
76. W. Harrison, K. Echelmeyer, C. Larsen, Measurement of temperature in a margin of Ice Stream B, Antarctica: Implications for margin migration and lateral drag. *J Glaciol.* **44**, 615–624 (1998).
77. C. Schoof, On the mechanics of ice-stream shear margins. *J. Glaciol.* **50**, 208–218 (2004).
78. J. Suckale, J. D. Platt, T. Perol, J. R. Rice, Deformation-induced melting in the margins of the West Antarctic ice streams. *J. Geophys. Res. Earth Surface* **119**, 1004–1025 (2014).
79. P. Hunter, C. Meyer, B. Minchew, M. Haseloff, A. Rempel, Thermal controls on ice stream shear margins. *J. Glaciol.* **67**, 435–449 (2021).
80. P. Duval, L. Arnaud, O. Brissaud, M. Montagnat, S. De La Chapelle, Deformation and recrystallization processes of ice from Polar ice sheets. *Ann. Glaciol.* **30**, 83–87 (2000).
81. M. F. Meier, *Mode of Flow of Saskatchewan Glacier Alberta, Canada, Geological Survey Professional Paper 351* (United States Government Printing Office, Washington, DC, 1960).
82. S. C. Colbeck, R. J. Evans, A flow law for temperate Glacier ice. *J. Glaciol.* **12**, 71–86 (1973).
83. T. G. Langdon, The physics of superplastic deformation. *Mater. Sci. Eng. A* **137**, 1–11 (1991).
84. L. Lliboutry, The dynamics of temperate Glaciers from the detailed viewpoint. *J. Glaciol.* **8**, 185–205 (1969).
85. G. Smith, L. Morland, Viscous relations for the steady creep of polycrystalline ice. *Cold Reg. Sci. Technol.* **5**, 141–150 (1981).
86. C. Wilson, Y. Zhang, K. Stüwe, The effects of localized deformation on melting processes in ice. *Cold Reg. Sci. Technol.* **24**, 177–189 (1996).
87. E. C. Pettit, T. Thorsteinsson, H. P. Jacobson, E. D. Waddington, The role of crystal fabric in flow near an ice divide. *J. Glaciol.* **53**, 277–288 (2007).
88. T. Chauve, M. Montagnat, P. Vacher, Strain field evolution during dynamic recrystallization nucleation: A case study on ice. *Acta Mater.* **101**, 116–124 (2015).
89. F. S. Graham, M. Morlighem, R. C. Warner, A. Treverrow, Implementing an empirical scalar constitutive relation for ice with flow-induced polycrystalline anisotropy in large-scale ice sheet models. *Cryosphere* **12**, 1047–1067 (2018).
90. R. B. Alley, J. Perepezko, C. Bentley, Grain growth in Polar ice: I. *Theory. J. Glaciol.* **32**, 415–424 (1986).
91. P. Duval, O. Castelnau, Dynamic recrystallization of ice in Polar ice sheets. *J. Phys.* **IV 05**, C3-197–C3-205 (1995).